Supplementary Materials for

Drop race: How electrostatic forces influence drop motion

Xiaomei Li[1], Pravash Bista[1], Amy Stetten[1], Henning Bonart[1,2], Maximilian T. Schür[2], Steffen Hardt[2], Francisco Bodziony[3], Holger Marschall[3], Alexander Saal[1], Xu Deng[4], Rüdiger Berger[1], Stefan Weber[1*], Hans-Jürgen Butt[1]*

[1] Max Planck Institute for Polymer Research, Ackermannweg 10, 55128 Mainz, Germany

[2] Institute for Nano- and Microfluidics, Technische Universität Darmstadt, Alarich-Weiss-Straße 10, 64287 Darmstadt, Germany

[3] Computational Multiphase Flows, Technische Universität Darmstadt, Alarich-Weiss-Straße 10, 64287 Darmstadt, Germany

[4] Institute of Fundamental and Frontier Sciences, University of Electronic Science and Technology of China, Chengdu, China.

This PDF file includes:

S1. Viscous dissipation due to hydrodynamic flow in the drop

The total viscous force of a sliding drop is commonly split in two components. One comes from the viscous dissipation in the bulk, F_b, the other is concentrated at the wedge, F_w. An upper limit for bulk viscous dissipation can be estimated by replacing a drop with its real 3D shape by drop with vertical side having a base area of $\pi lw/2$ and a height H. We assume that the bottom area of the drop is stationary (no slip) and that the top area at height H is sliding with $2U$. Twice the velocity to ensure that the center moves with U. Then, the bulk viscous force is:

$$F_b \approx \eta \frac{\pi lw}{2H} U \qquad \text{(S1)}$$

This is more an upper limit. Le Grand, Daerr & Limat use $F_v = \eta U V^{1/3}$ [1]. Kim, Lee & Kang apply $F_v = \eta \pi r_d^2 U/H$ [2]. Here, V is the volume of the drop and r_d is the radius of the contact area of a drop, which, for simplicity, is assumed to have a circular contact radius.

In addition to bulk viscous dissipation, there is viscous dissipation in the wedge region [2-10]. Since we observe the shape of drops with a camera at a resolution of ≈10 µm, we detect macroscopic contact angles $\Theta_a(U)$ and $\Theta_r(U)$. Viscous dissipation in the wedge happens at a shorter length scale and manifests itself in an increase of $\Theta_a(U)$ and a decrease of $\Theta_r(U)$. Therefore, it is already included in Eq. (1).

S2. Experimental setup and image analysis

The experimental setup is shown in Figure S1. To extract L, $\Theta_a(L)$, $\Theta_r(L)$, and w from the videos, we used and adapted the freely available drop shape analysis from MATLAB (DSAfM) originally developed by Andersen & Taboryski [11] (for details see [12]). In a first step, images without a drop and the images with complete drops are identified. The images without a drop are used to extract the tilt angle. The images with a complete drop were corrected by subtracting the background and then rotating into a horizontal drop. Then the contour, front edge position and rear edge position of the drops were detected with sub-pixel precision. By the distance between rear edge and front edge, we calculated the length of the drop from side view and the width of the drop from front view. Afterwards, the image was divided into the front half and the rear half of the drop to further analyse the advancing and receding contact angles and the respective velocity. The velocities of both sides were calculated by the rear and front edge point moving distance in each frame. Dynamic contact angles were determined by applying a 4th order polynomial fit to the counter of drop in each image. To get the height of drops, we employ a free software named "Tracker" (https://github.com/OpenSourcePhysics/tracker). By defining the distance between the above drop edge and the highest point of a drop as the drop height, then setting the highest point of a drop as the tracking point, we got the real-time height of drops. All measurements were conducted at a temperature of 20±1°C and a humidity of 15-30%.

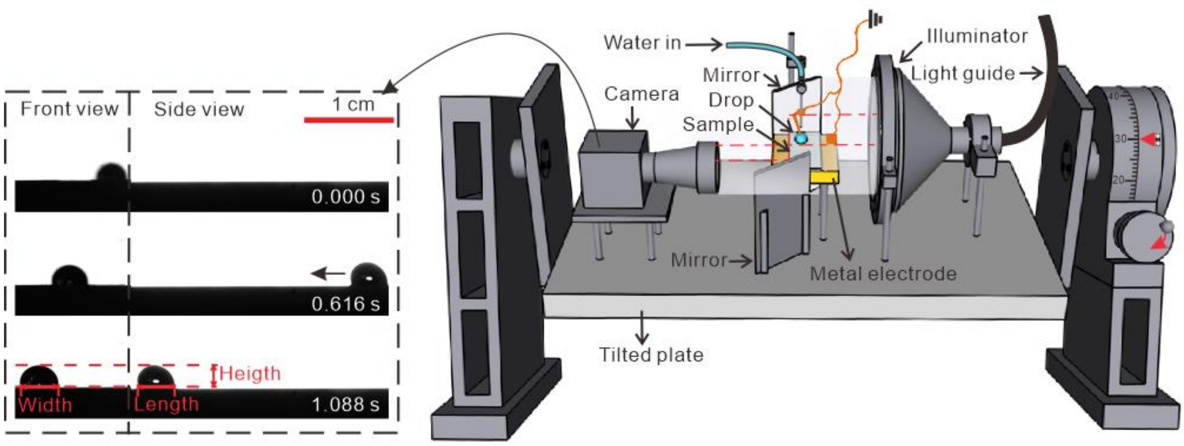

***Figure S1**. Experimental setup. Water drops were automatically placed from a grounded syringe needle which was connected to a peristaltic pump onto the top of the tilted plate at fixed time intervals of 1.3 s. They contacted a grounded electrode and then started to move down the plate. The slide length and time were set to zero when drops detached from the electrode. At this point they unavoidably already had a velocity U_0. Sliding drops were imaged with a camera in side and front view by using two parallel mirrors. From side-view images, the positions of the front and rear contact lines, drop velocity, dynamic advancing Θ_a, receding contact angles Θ_r and the length of the drops were determined. For details about data processing, we refer to [12].*

S3. Static advancing and receding contact angles

Table S1*. Receding Θ_r^0 and advancing contact angles Θ_a^0 and contact angle hysteresis, $\Delta\Theta = \Theta_a^0 - \Theta_r^0$ for the hydrophobic samples studied.*

Coating	Substrate	Name of surfaces	Θ_r^0	Θ_a^0	$\Delta\Theta$
PFOTS	Si	PFOTS-on-Si	87	117	30
	1 mm SiO_2	PFOTS-on-1mm-SiO_2	85	115	30
	5 mm SiO_2	PFOTS-on-5mm-SiO_2	86	116	30
Polystyrene (20 nm)	Gold	PS-on-gold	80	97	17
	1 mm SiO_2	PS-on-1mm-SiO_2	77	93	16
	5 mm SiO_2	PS-on-5mm-SiO_2	78	95	17
Teflon AF 1600 (60 nm)	Gold	Teflon-on-gold	109	122	13
	1 mm SiO_2	Teflon-on-1mm-SiO_2	110	122	12
	5 mm SiO_2	Teflon-on-5mm-SiO_2	110	121	11
PDMS brushes	Si	PDMS-on-Si	88	105	17
	1 mm SiO_2	PDMS-on-1mm-SiO_2	86	105	19
	5 mm SiO_2	PDMS-on-5mm-SiO_2	87	102	15
Perfluoro-decanethiols	Gold	Thiols-on-gold	95	115	20

S4. Scanning force microscope imaging

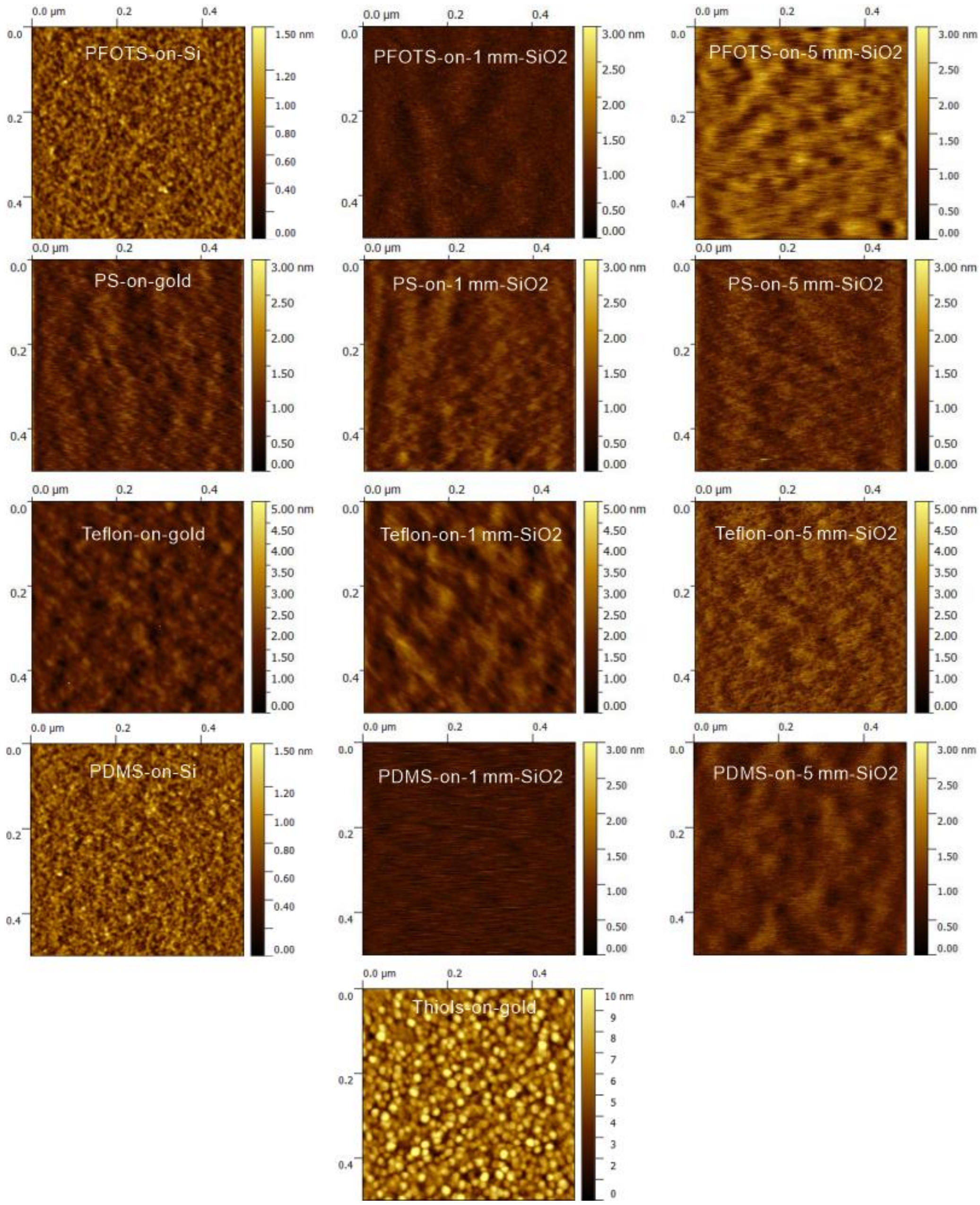

Figure S2. *SFM tapping mode images of all hydrophobic surfaces.*

S5. Drop velocity-versus-slide length for PFOTS-coated surfaces at different tilt angles

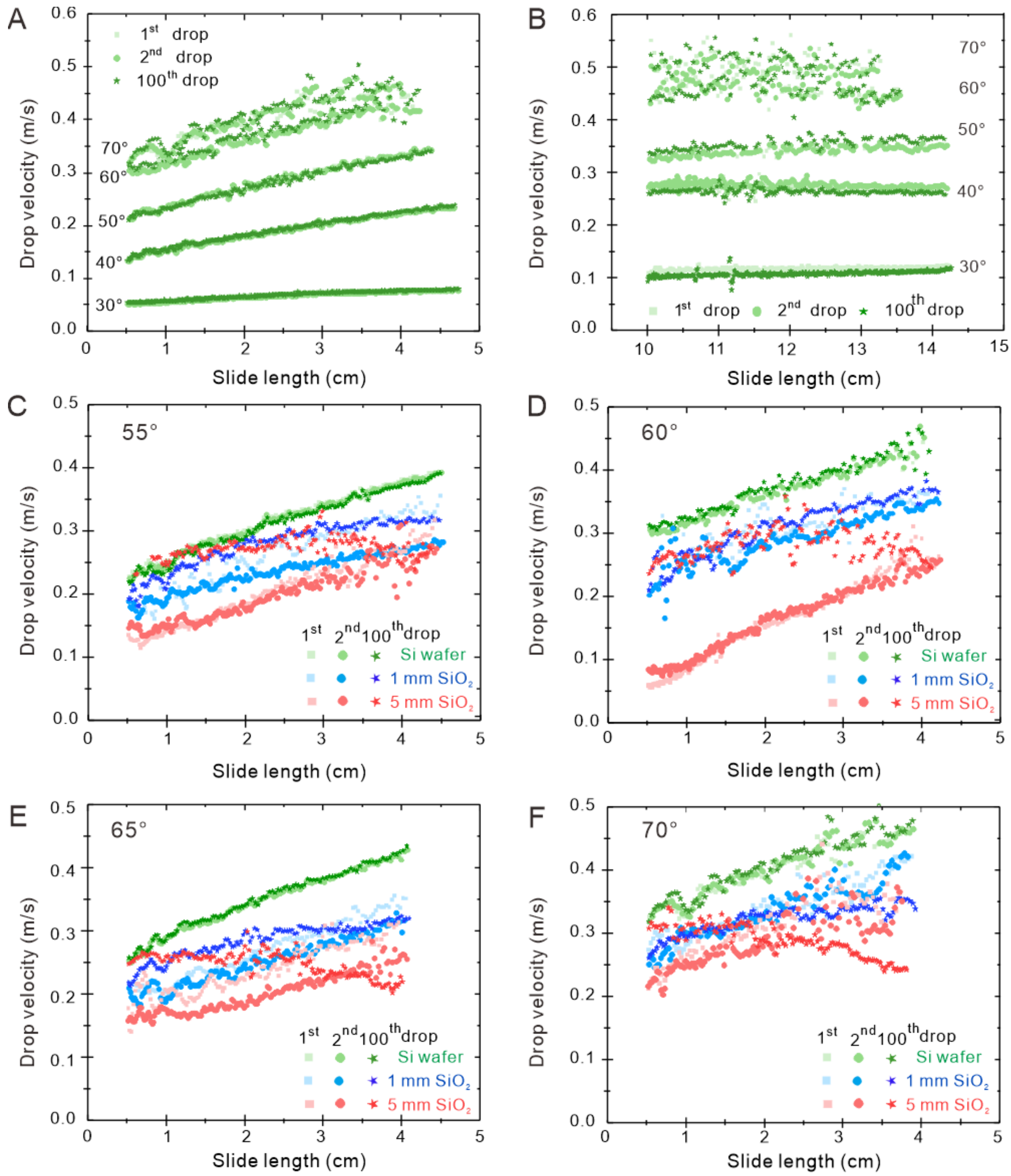

***Figure S3**. Representative results for drop velocity-versus-slide length for 33 µL water drops on PFOTS-coated samples. Drops sliding on PFOTS-on-Si the first 5 cm (A) and after having already moved 10 cm (B) at different tilt angles. (C-F) Drops on PFOTS on Si wafer (green symbols), 1 mm SiO_2 (blue symbols) and 5 mm SiO_2 (red symbols) deposited at a rate of one drop per 1.3 s measured at 55° (C), 60° (D), 65° (E), and 70° (E) tilt angles. For comparison also the results obtained on Si wafers are plotted as green symbols. Results for drop number 1 (rectangles), 2 (circles), and 100 (stars) are plotted.*

S6. Direct numerical diffuse interface simulations of drop motion

Due to the no-slip boundary condition on solid surfaces drops show a rolling component in their motion [13-19]. To quantify the effective mass of the rolling drop, Direct Numerical Simulations (DNS) [20] deploying a diffuse interface phase-field method were performed. The effective mass is defined by $m^* = 2E_{kin}/U^2$, where E_{kin} is the kinetic energy of the drop. In our DNS, the interface was treated as a diffuse layer through which the fluid properties vary steeply but continuously. On the mesoscopic scale, the motion of the contact line occurs naturally as diffusion across the interface driven by gradients of the chemical potential. In contrast, the conventional sharp-interface model suffers from a non-integrable stress singularity at the sliding contact line [21,22].

The results of simulations for three-dimensional droplets on an inclined wall were obtained with phaseFieldFoam, a diffuse interface phase-field solver developed within the OpenFOAM C++ library for computational continuum physics [23,24]. The solver has also been enhanced to use a sliding reference-frame technique, to follow the droplet's centre-of-mass, effectively reducing the computational effort.

The following properties of the air-water system were used for the simulations: Water density ρ = 1000 kg/m^3, water dynamic viscosity η = 10^{-3} Pas, air density ρ_a = 1 kg/m^3, air dynamic viscosity η_a = 10^{-5} Pas, surface tension of water γ = 0.072 N/m. A no-slip boundary condition is applied at the bottom boundary with free-slip boundary conditions being applied on every other boundary.

For initialization, a hemispherical drop with radius R = 2.5 mm (V = 32.7 µL, contact angle of 90°) was placed on a 25×10 mm^2 rectangular domain at (0.0125, 0) m, on a smooth inclined wall. For various inclination angles, the droplet's barycentre position and velocity have been tracked and its kinetic energy density field has been measured. This allowed to calculate both contributions to the total kinetic energy – the translational and rotational kinetic energies.

The factor m^*/m slightly changed as a function of barycentre velocity (Figure S4). Initially, the so-called sliding acceleration is greater than the rotational one, leading to a slow increase of m^*/m since the main contribution to the total kinetic energy is from the sliding. The change in slope is more pronounced for lower inclination angles since the sliding acceleration is also lower, when compared to larger inclination angles. After some time, the droplet's sliding acceleration starts to decrease but its angular acceleration is still increasing. Therefore, a steeper increase of m^*/m was observed. Since our calculations of the electrostatic force did not depend sensitively on the precise value of m^*/m, we applied the value of 1.05 throughout our analysis.

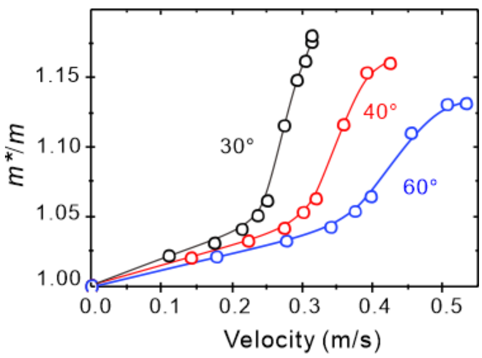

***Figure S4**. Effective mass m* divided by real mass m of the drop versus velocity of a 32.7 µL water drop with an initial contact angle of 90° at tilt angles of 30°, 40°, and 60°.*

S7. Aspect ratio of drops

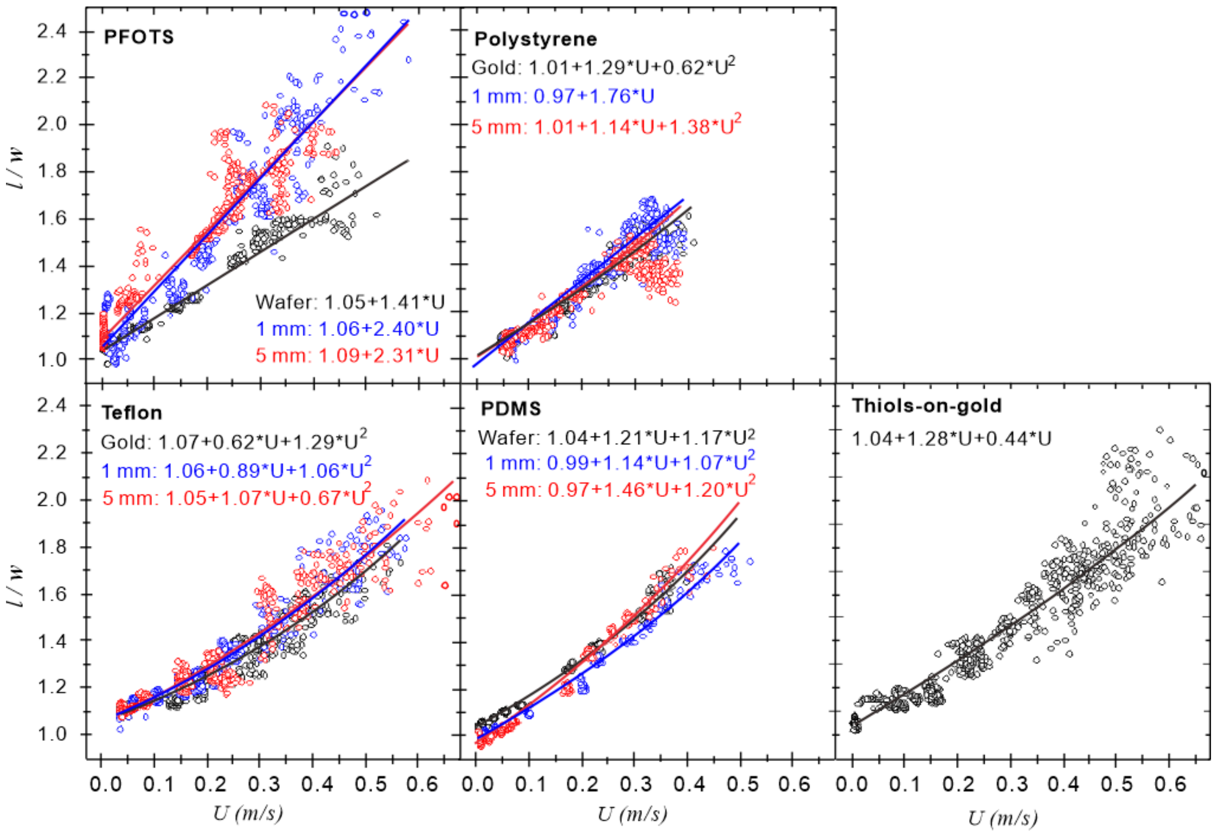

***Figure S5**. Ratio of length-to-width of the contact area of sliding water drops l/w versus drop velocity U on different surfaces. The corresponding experiments were carried out at different tilt angles to span a large velocity range. The equations give the best fits. In some cases, linear fits were sufficient. In others we used 2^nd^ order polynomial fits.*

S8. Contribution of capillary and bulk viscous force

Although for the analysis of electrostatic force we do not need to know the origin of the reference force, it is still instructive to see how significantly capillary and viscous forces contribute. Therefore, we inserted the respective drop widths, advancing, and receding contact angles into Eq. (1) with $k = 1$, calculated the capillary force (Figure S6, red symbols) and compared it to measured reference forces (Figure S6, black symbols). Capillary forces, which include wedge viscous forces (see SI1), dominate over bulk hydrodynamic viscous forces calculated with Eq. (2) (Figure S6, blue symbols).

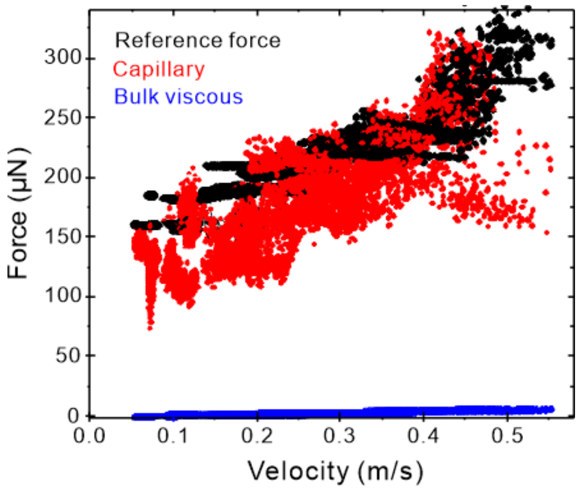

Figure S6. *Force acting on 33 µL water drops sliding down PFOTS-on-Si versus velocity. Reference forces were calculated with* $mg\sin\alpha - m^{*}\frac{dU}{dt}$ *(black symbols) for the respective 2nd and 10th drop for tilt angles ranging from 30° to 70°. Capillary forces were calculated with Eq. (1) and k=1. Bulk viscous forces calculated with Eq. (2) (blue). Results of three experiments are plotted. To complete the graphs in particular at high velocity we added results obtained from 10-14 cm slide distance, where the drops were close to their steady-state velocity.*

S9. Measured extra force on PFOTS-coated substrates

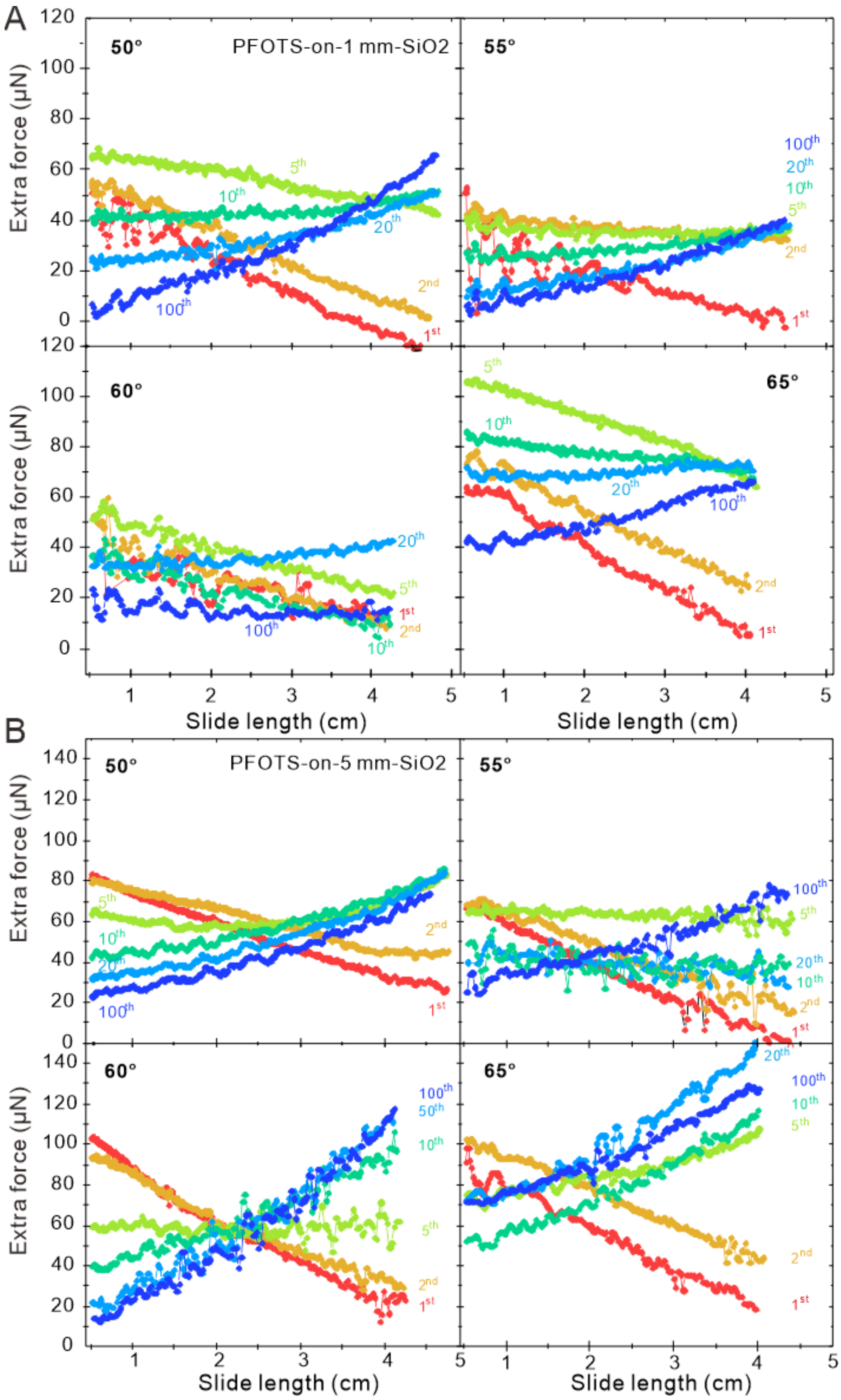

Figure S7. Representative extra force acting on water drops on PFOTS-on-1mm-SiO_2 (A) and PFOTS-on-5mm-SiO_2 (B) measured at different tilt angles. Plotted are results for the 1^{st}, 2^{nd}, 5^{th}, 10^{th}, 20^{th}, 50^{th} and 100^{th} drop. 33 μL drops were deposited at an interval of 1.3 s. Forces were calculated with Eq. (4) with m^*/m=1.05 and $F_r(U) = 156\mu N + 218\frac{\mu Ns}{m}U$.

S10. Measurement of drop charges

Drop charges were measured with a tilted plate setup at fixed tilt angle of 50° (details in [25]). Right after deposition, water drops were discharged by touching a grounded electrode at the beginning of their slide path at $L = 0$. After sliding 4 cm, a second electrode measured the drop discharge current via a variable gain sub femto current amplifier (response time: 0.8 ms, DDPCA-300, FEMTO). To reduce noise, the setup was placed in a Faraday cage. Care was taken that the drop disconnected from the electrode before rolling over the end of the sample into a collection dish. Data was recorded using a National Instruments data acquisition card (NI USB-6366 X-Series) and the accompanying LabVIEW software. 45 µL drops were run successively over the surface. A current spike was recorded when each drop touched the electrode (Figure S8). The drop charge was calculated by integrating the current signal over the first 2 ms. Experiments were carried out at a temperature of 21±1°C and a relative humidity of 15-30%.

The charge of the first drop in a series Q_1 was the highest (Figure S9). For the following drops, we measured monotonically decreasing charges. After typically 10-50 drops a saturation charge Q_∞ was reached (table S2). Q_1 and Q_∞ depend on the specific sample and varied by 30%-50% from sample to sample. A possible reason for this variation could be the surface quality of a particular batch, lab temperature, or humidity on the day of the experiment. To get a first estimate of the initial surface charge density σ_0, the decay length λ, and the neutralization time τ, we used the methods and the charging model developed in [25]. The uncertainty from the charge measurement propagated to the estimation of drop charging parameters. We refined these parameters by comparing the experimental first and 100th drop force-vs-slide length curves with predictions by Eqs. (S14) and (S21), respectively.

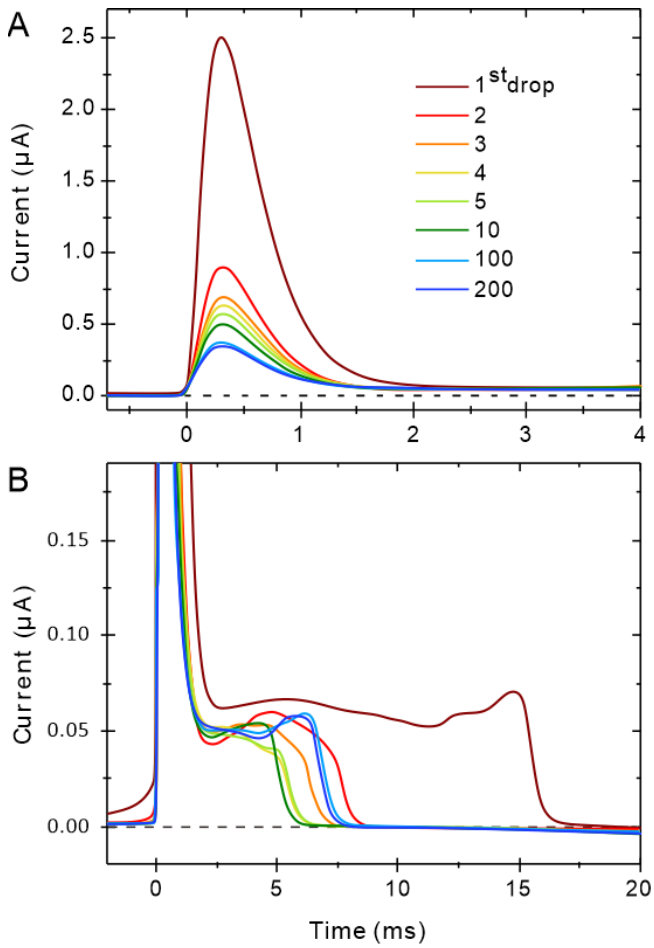

***Figure S8**. Typical current traces detected for a series of 45 µL water drops on PFOTS-on-1mm-SiO_2 after sliding 4 cm. Currents are plotted at different scales. As the probe electrode touches a sliding drop at $t = 0$, it discharges the accumulated drop charge within 2 ms, causing a positive current peak. This positive peak is due to the flow of electrons towards the positively charged drop, which also implies a negatively charged surface. The total accumulated drop charge was calculated by integrating the initial current peak of 2 ms. While the drop passes the probe electrode, a steady-state current of ≈0.05 µA is generated (B).*

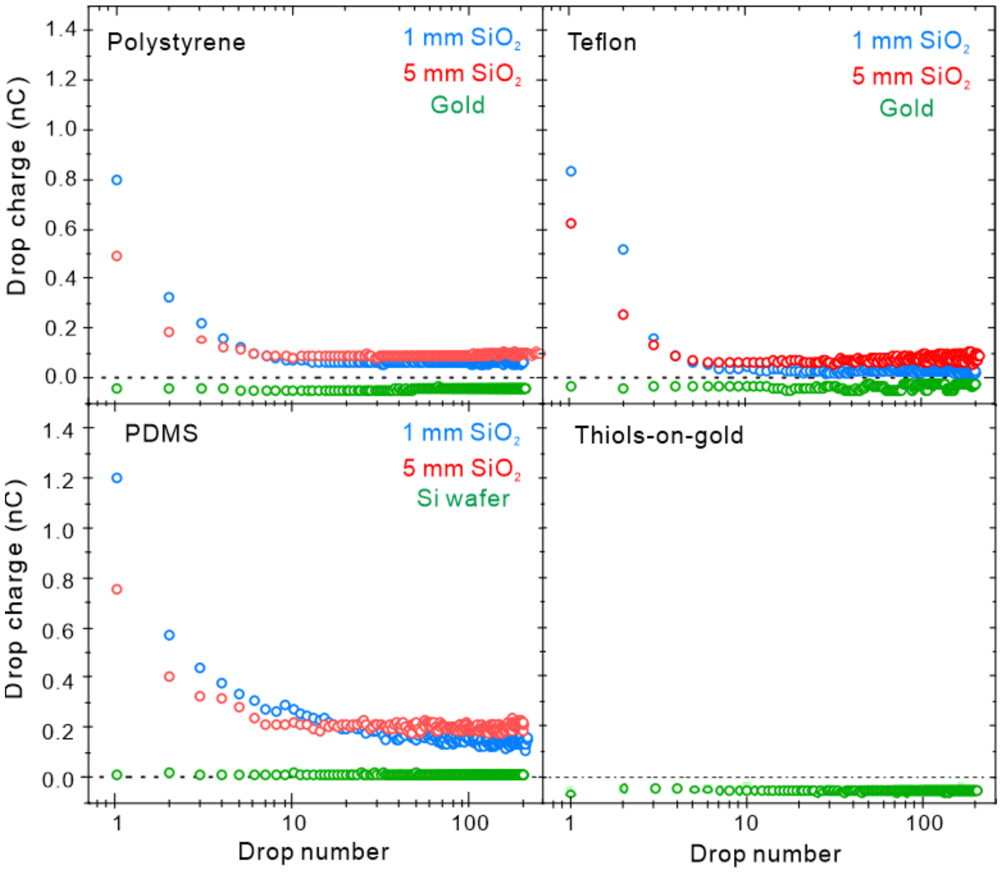

Figure S9. *Measured drop charge-versus-drop number on 20 nm polystyrene films, 60 nm Teflon films, PDMS-brushes on different substrates and monolayers of Perfluorodecanethiol on gold. Results were measured at 50° tilt, 1.5 s intervals between deionized water drops of 45 µL volume after 4 cm slide length.*

On all SiO_2 substrates drops gained a positive charge and deposited a negative charge on the surfaces. In contrast, on silicon wafers or gold, drop charges were much lower. Charge separation was highest on PFOTS-coated SiO_2 followed by PDMS and the polymer films. The saturated drop charge, Q_∞ increased between the 1 mm and 5 mm SiO_2 substrates. This effect was most pronounced on PFOTS. On silicon wafers charging was ≈10 times lower. On gold, the drop charge was even negative. The measured charge values agree well with earlier experiments on PFOTS-coated glass slides [25] and other hydrophobic surfaces.

Table S2. Mean charge of the first drop and drops in steady state in series with 1.5 s time interval between them. V = 45 µl, α = 50°, 4 cm slide distance, T = 21±1°C, RH = 15-30%.

Surfaces	Q_1 nC	Q_∞ nC	τ s	λ cm	σ_0 µC/m^2
PFOTS-on-Si	0.18	0.09			
PFOTS-on-1 mm-SiO_2	1.4	0.26	12	2	-20
PFOTS-on-5 mm-SiO_2	1.4	0.45	7	1.5	-20
PS-on-gold	-0.03	-0.04			
PS-on-1 mm-SiO_2	0.7	0.05	30	2.5	-10
PS-on-5 mm-SiO_2	0.5	0.07	17	2	-7
Teflon-on-gold	-0.03	-0.02			
Teflon-on-1 mm-SiO_2	0.7	0.05	70	2.8	-10
Teflon-on-5 mm-SiO2	0.7	0.07	20	3	-7
PDMS-on-Si	0.02	0.02			
PDMS-1 mm-SiO_2	1.2	0.15	12	4	-12
PDMS-5 mm-SiO_2	0.6	0.2	8	0.9	-12
Thiols-on-gold	-0.05	-0.05			

S11. Analytical approximation of the electrostatic force on a drop

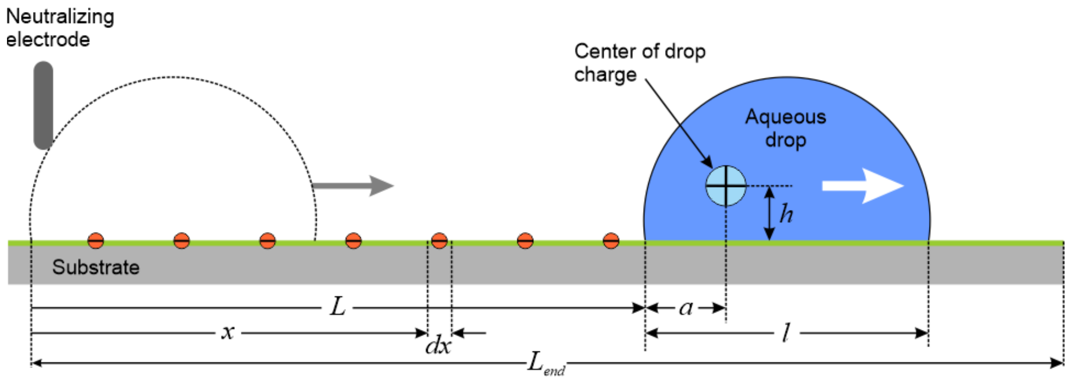

Figure S10. *Parameters used to calculate the electrostatic force.*

We derive an expression for the force between a drop bearing a charge Q interacting with a stripe of surface charges σ distributed over its track of slide length L. We assume the center of charge of the drop to be at a distance a from the rear side and at a height h (Figure S10). To obtain the electrostatic force we consider the electric field generated by a charge deposited at the solid-air interface on top of an infinitely extending solid half space (eq. 3). A surface charge dq at position x generates an electric field with lateral component

$$dE(x,h) = \frac{dq}{2\pi\varepsilon_0(\varepsilon_S+1)}\frac{L+a-x}{[(L+a-x)^2+h^2]^{3/2}} \quad . \tag{S4}$$

This is the field strength at a position $L+a$ along the surface and a height h above the solid surface. Along its path, the drop deposits a certain surface charge density $\sigma(x)$. Since the local charge density may vary in a direction perpendicular to the slide direction, σ is taken to be the mean charge density at position x. The deposited charge can be related to the surface charge density on the free solid surface by $dq = \sigma w dx$, where w is the width of the contact area of the drop. Integrating the Coulomb forces of all infinitesimal charge elements dq gives the total lateral force on the drop:

$$F_e^n(L) = \frac{wQ(L)}{2\pi\varepsilon_0(\varepsilon_S+1)}\left[\int_0^L \frac{(L+a-x)\sigma(x)}{((L+a-x)^2+h^2)^{3/2}}dx - \int_{L+l}^{L_{end}} \frac{(x-L-a)\sigma\prime(x)}{((x-L-a)^2+h^2)^{3/2}}dx\right] \tag{S5}$$

Assuming that $h << L+a-x$ we get Eq. (5). Here, the sign convention is that a positive force is decelerating the drop. The second term in (S5) takes into account surface charges $\sigma'(x)$ situated ahead of the drop which is different from the charge distribution $\sigma(x)$ behind the drop.

To evaluate Eq. (S5), we need to make an assumption about the surface charge distribution. The simplest case is to assume that the drop only interacts with charges deposited by itself. This is the case for the first drop in a series. We further assume that the surface charge density is constant and that no charge on the surface and inside the drop is neutralized. Then, the charge of the first drop is $Q_1 = -Lw\sigma_1$, leading to an electrostatic force of

$$F_e^1(L) = -\frac{Lw^2\sigma_1^2}{2\pi\varepsilon_0(\varepsilon_S+1)}\left[\frac{1}{\sqrt{a^2+h^2}} - \frac{1}{\sqrt{(L+a)^2+h^2}}\right] \quad . \tag{S6}$$

We used the superscript "1" to indicate that this is the first drop sliding down an initially neutral surface. σ_1 is the surface charge density deposited by the first drop.

A constant surface charge density is, however, not realistic. More realistic is a charge density that saturates exponentially with slide distance [25]. Again, considering the first drop and assuming that a drop only interacts with charges deposited by itself, the corresponding surface charge density and total charge of the drop can be parametrized as

$$\sigma_1 = \sigma_0 e^{-x/\lambda} \text{ and } Q_1 = -w\lambda\sigma_0\left(1 - e^{-L/\lambda}\right) \qquad \text{(S7)}$$

Here we assumed that a possible neutralization of the surface is very slow compared to the sliding time of the drop. Inserting these two expressions into the first term of Eq. (5) leads to

$$F_e^1(L) = -\frac{w\lambda\sigma_0\left(1-e^{-L/\lambda}\right)w\sigma_0}{2\pi\varepsilon_0(\varepsilon_S+1)}\int_0^L \frac{e^{-x/\lambda}}{(L+a-x)^2}dx = -C\left(1 - e^{-L/\lambda}\right)\int_0^L \frac{e^{-x/\lambda}}{(L+a-x)^2}dx \qquad \text{(S8)}$$

The second term in Eq. (5) was not considered because we only take the charge deposited by the drop into account; thus, there is no charge ahead of the drop. Here, the constant $C = w^2\sigma_0^2\lambda/[2\pi\varepsilon_0(\varepsilon_S + 1)]$ summarizes all distance-independent parameters. Partial integration yields

$$F_e^1(L) = -C\left(1 - e^{-L/\lambda}\right)\left\{\left[-\frac{e^{-x/\lambda}}{L+a-x}\right]_0^L - \frac{1}{\lambda}\int_0^L \frac{e^{-x/\lambda}}{L+a-x}dx\right\} \qquad \text{(S9)}$$

Substitution with $t = \frac{L+a-x}{\lambda}$ gives

$$F_e^1(L) = C\left(1 - e^{-L/\lambda}\right)\left\{\frac{1}{a}e^{-\frac{L}{\lambda}} - \frac{1}{L+a} - \frac{1}{\lambda}e^{-\frac{L+a}{\lambda}}\int_{(L+a)/\lambda}^{a/\lambda}\frac{e^t}{t}dt\right\} \qquad \text{(S10)}$$

The integral in Eq. (S10) has the form of the exponential integral function:

$$\mathrm{Ei}(z) = \int_{-\infty}^{z}\frac{e^t}{t}dt \qquad \text{for } z > 0 \qquad \text{(S11)}$$

With this function, we can calculate the force as

$$F_e^1(L) = C\left(1 - e^{-L/\lambda}\right)\left\{\frac{1}{a}e^{-\frac{L}{\lambda}} - \frac{1}{L+a} - \frac{1}{\lambda}e^{-\frac{L+a}{\lambda}}\left[Ei\left(\frac{a}{\lambda}\right) - Ei\left(\frac{L+a}{\lambda}\right)\right]\right\} \qquad \text{(S12)}$$

To evaluate this expression, the series representation of the exponential integral can be employed,

$$\mathrm{Ei}(z) = 0.5772 + \ln(|z|) + \sum_{n=1}^{\infty}\frac{z^n}{n!\,n}, \qquad \text{(S13)}$$

where 0.5772 is the Euler-Mascheroni constant. Using Eq. (S13), we can write

$$F_e^1(L) = \frac{C}{\lambda}\left(1 - e^{-L/\lambda}\right)\left\{\frac{\lambda}{a}e^{-\frac{L}{\lambda}} - \frac{\lambda}{L+a} - e^{-\frac{L+a}{\lambda}}\left[\ln\left(\frac{a}{L+a}\right) + \sum_{k=1}^{\infty}\frac{a^k-(L+a)^k}{\lambda^k k!k}\right]\right\} \qquad \text{(S14)}$$

For large arguments, convergence of this series can be slow. For example, to reach an accuracy of 5% and 1% at z = 5 one needs to take n = 8 and 10 terms, respectively. For z = 10 the series needs to be considered up to n = 14 and 16, respectively. Many modern mathematical programs, such as Wolfram Alpha or IgorPro (Wavemetrics) provide built-in functions for the effective numerical computation of the exponential integral function.

The distance-dependent part of Eq. (S14) (Dimensionless force) is plotted in figure S11A. A maximum is observed at $L/\lambda \approx 0.8$. The force decreases with increasing a/λ; thus, the more the center of charge is shifted towards the rear of the drop, the stronger the electrostatic retardation becomes. This strong dependence on a/λ results from interactions with surface charges in the close vicinity of the drop, for which the analytical model is not realistic. To better quantify these near-field interactions, we have developed the numerical model described in the following section. In terms of the analytical model, a is regarded as a parameter that describes the near-field interactions in an effective manner.

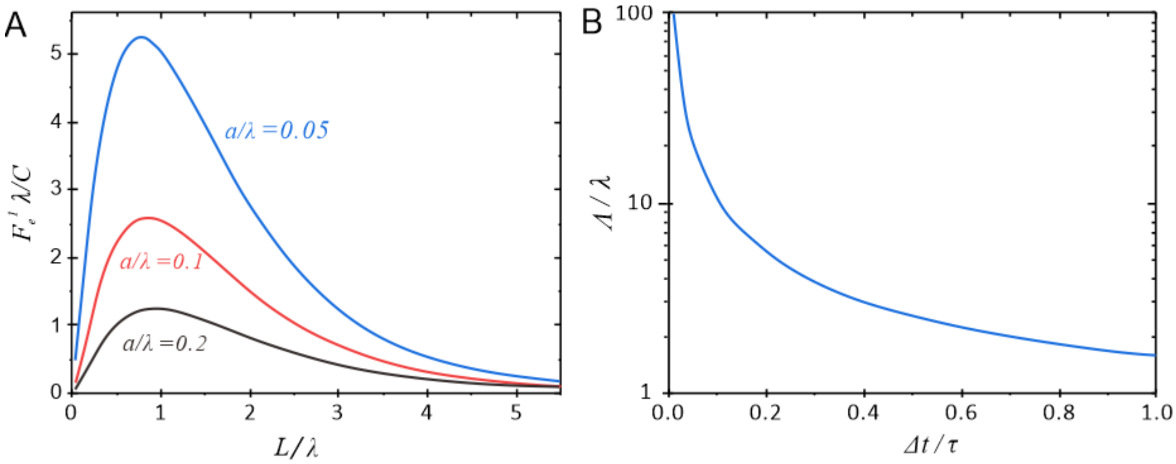

Figure S11. *(A) Plot of dimensionless force $F_e^1\lambda/C$ versus L/λ for $a/\lambda = 0.05$, 0.1 and 0.2 calculated with Eq. S14. (B) Ratio of Λ/λ-versus-$\Delta t/\tau$ calculated with Eq. (S15).*

For a succession of drops sliding over the surface at time intervals Δt, the charge distribution and the drop charge are altered by the presence of surface charges of previous drops. Once deposited, the surface charge is neutralized with a characteristic neutralization time τ. To calculate the charge distribution for following drops, a recursive approach is required. Thus, a closed analytical description for the electrostatic force on successive drops is difficult. Nevertheless, a relatively simple analytical description is possible for the saturated drop charge distribution after a large number ($n \to \infty$) of drops. Here, the surface charge density and the drop charge are given by [25]:

$$\sigma_\infty(x) = \sigma_0 e^{-x/\Lambda},\ Q_\infty(L) = -\sigma_0 \lambda w\left(1 - e^{-L/\Lambda}\right) \text{ with } \Lambda = \frac{\lambda}{1-e^{-\Delta t/\tau}} \quad . \qquad \text{(S15)}$$

For short time intervals the modified saturation distance, Λ, is much larger than the initial saturation distance, λ (Figure S11B). With increasing drop interval time, $\Delta\tau$, Λ decreases and eventually approaches the initial λ for $\Delta t/\tau \gg 1$.

Using these expressions, we calculate the electrostatic force caused by the charges behind the drop in analogy to Eq. (S14):

$$F_{eb}^{\infty}(L) = \frac{C}{\Lambda}\left(1 - e^{-L/\Lambda}\right)\left\{\frac{\Lambda}{a}e^{-\frac{L}{\Lambda}} - \frac{\Lambda}{L+a} - e^{-\frac{L+a}{\Lambda}}\left[Ei\left(\frac{a}{\Lambda}\right) - Ei\left(\frac{L+a}{\Lambda}\right)\right]\right\}$$

$$= \frac{C}{\Lambda}\left(1 - e^{-L/\Lambda}\right)\left\{\frac{\Lambda}{a}e^{-\frac{L}{\Lambda}} - \frac{\Lambda}{L+a} - e^{-\frac{L+a}{\Lambda}}\left[\ln\left(\frac{a}{L+a}\right) + \sum_{k=1}^{\infty}\frac{a^k-(L+a)^k}{\Lambda^k k! k}\right]\right\} \tag{S16}$$

In addition, surface charges ahead of the drop are accelerating the drop. Their contribution is given by

$$F_{eb}^{\infty}(L) = \frac{\sigma_0^2 w^2 \lambda}{2\pi\varepsilon_0(\varepsilon_S+1)}e^{-\Delta t/\tau}\left(1 - e^{-L/\lambda}\right)\int_{L+l}^{L_{end}}\frac{\sigma}{(x-L-a)^2}dx$$

$$= Ce^{-\Delta t/\tau}\left(1 - e^{-L/\Lambda}\right)\int_{L+l}^{L_{end}}\frac{e^{-x/\Lambda}}{(x-L-a)^2}dx\ . \tag{S17}$$

The factor $e^{-\Delta t/\tau}$ takes into account that after the time interval Δt the charge left by the previous drop has been partially neutralized.

Partial integration and substitution with $t = -(x - L - a)/\Lambda$ gives

$$F_{eb}^{\infty}(L) = Ce^{-\Delta t/\tau}\left(1 - e^{-L/\lambda}\right)\left\{\left[\frac{e^{-x/\lambda}}{x-L-a}\right]_{L+l}^{L_{end}} + \frac{1}{\Lambda}e^{-\frac{L+a}{\Lambda}}\int_{-(l-a)/\Lambda}^{-(L_{End}-L-a)/\Lambda}\frac{e^t}{t}dt\right\} \tag{S18}$$

Here, the argument of the exponential integral as defined in Eq. (S11) is negative. We therefore have to use the following function

$$\mathrm{Ei}(-\mathrm{z}) = -\mathrm{E}_1(z) = -\int_z^{\infty}\frac{e^{-t}}{t}dt \qquad \text{for } z > 0 \tag{S19}$$

Where $E_1(z)$ is defined as

$$\mathrm{E}_1(z) = -0.5772 - \ln(|\mathrm{z}|) - \sum_{n=1}^{\infty}\frac{(-z)^n}{n!\,n}$$

Using these definitions, we get:

$$F_{eb}^{\infty}(L) = \frac{C}{\Lambda}e^{-\Delta t/\tau}\left(1 - e^{-L/\lambda}\right)\left\{\frac{\Lambda \mathrm{e}^{-\mathrm{L_{end}}/\Lambda}}{L_{end}-L-a} - \frac{\Lambda \mathrm{e}^{-\frac{\mathrm{L+l}}{\Lambda}}}{l-a} - e^{-\frac{L+a}{\Lambda}}\left[E_1\left(\frac{L_{End}-L-a}{\Lambda}\right) - E_1\left(\frac{l-a}{\Lambda}\right)\right]\right\}$$

$$= \frac{C}{\Lambda}e^{-\Delta t/\tau}\left(1 - e^{-L/\lambda}\right)\left\{\frac{\Lambda \mathrm{e}^{-\frac{\mathrm{L_{end}}}{\Lambda}}}{L_{end}-L-a} - \frac{\Lambda \mathrm{e}^{-\frac{\mathrm{L+l}}{\Lambda}}}{l-a} - e^{-\frac{L+a}{\Lambda}}\left[\ln\left(\frac{l-a}{L_{end}-L-a}\right) + \sum_{k=1}^{\infty}\frac{(L_{end}-L-a)^k-(l-a)^k}{\Lambda^k k! k}\right]\right\}$$

(S20)

The total electrostatic force acting on drop number $n > 50$ is the sum of both contributions:

$$F_e^{\infty}(L) = F_{ea}^{\infty}(L) + F_{eb}^{\infty}(L) \quad \text{for } L < L_{end} - l. \tag{S21}$$

The different contributions to the total force are shown in Figure S12 Interestingly, the accelerating force of the charges ahead of the drop is stronger at the beginning before the decelerating force of the charges behind the drop start to dominate. At the end of the slide path, there are no more charges ahead and the accelerating force contribution vanishes at $L_{end} - l$, leading to a steep increase in the drop force.

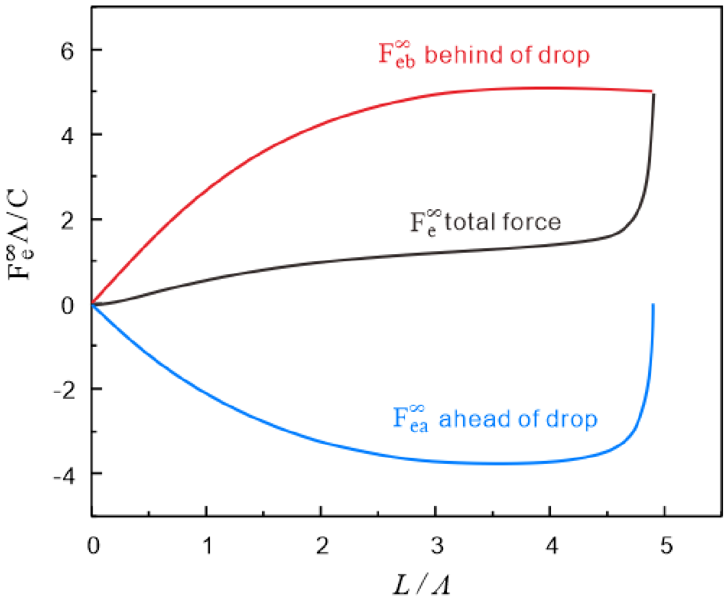

Figure S12. *Dimensionless force $F_e^{\infty}\Lambda/C$ on a drop after a long (>50) succession of drops as a function of slide length normalized with respect to the saturation length, L/Λ. The total force acting on the drop (black curve) consists of an accelerating force coming from charges ahead of the drop (blue curve) and a decelerating force from charges behind the drop (red curve). Parameters used in this example: Λ = 4 cm, w = 4 mm, l = 5 mm, a = 2 mm, L_{end} = 20 cm.*

S12. Numerical computation of the electrostatic force on a drop

One of the assumptions in Eq. (5) was to neglect the presence of the grounded back-electrode. To account, among other things, for the presence of the back electrode, we carried out numerical calculations of the electric field distribution based on Poisson's equation and the electrostatic force. As it turned out, by choosing the position of the center of charge in the drop appropriately we can account for the presence of the back electrode. In figure S13 the two-dimensional simulation domain and the mesh are displayed. The domain includes the substrate, the drop, and the surrounding air.

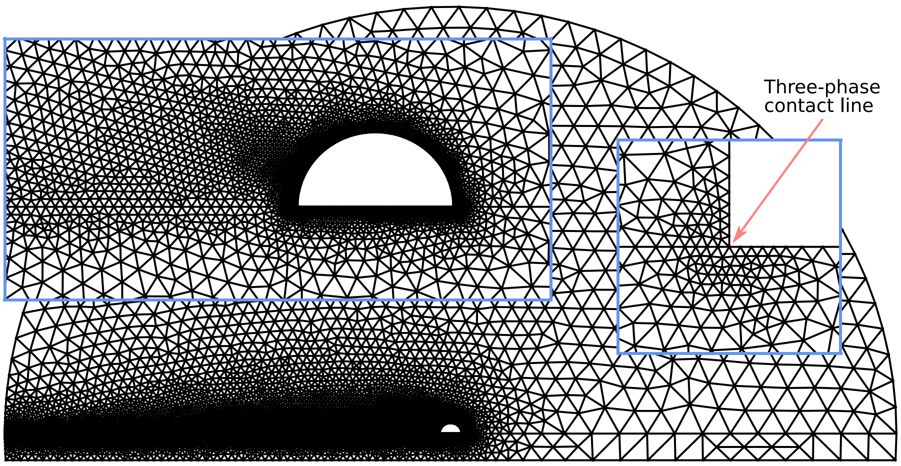

Figure S13*. Overview of the simulation domain and the grid including the substrate, the drop, and the surrounding air, compare figure S10. The insets display the finer mesh around the drop and the highly refined mesh around the contact line (the physical height shown in the latter inset is 1* µm*).*

The fundamental equation of electrostatics is Gauss's law. If the media are linear, isotropic, homogeneous and do not carry a space charge we end up with Poisson's equation $\Delta\varphi = 0$ in the surrounding air and in the substrate, with appropriate boundary conditions at the interfaces between different materials.

We assume that the drop is a conductor and can be modelled as a surface with a constant potential φ_{drop}. Even for non-conductive bodies with a dielectric permittivity much higher than their surrounding (such as water) this boundary condition is a good approximation. The value of φ_{drop} cannot be specified directly but is given implicitly by the total charge of the drop Q. Q and φ_{drop} are related by solving Poisson's equation and integrating $\int_{drop} \varepsilon_0 \vec{E} \cdot \vec{n} ds$ along the surface of the drop; here ε_0 is the vacuum permittivity and $\vec{n}$ and ds are the normal vector and the infinitesimal line element along the drop's surface, respectively. To fix the potential on the drop's surface, we iteratively vary φ_{drop} until the calculated drop charge is equal to the real drop charge.

At the interface between the substrate and air the electric field needs to fulfil the boundary condition $-(\varepsilon_s \vec{\nabla}\varphi_s - \vec{\nabla}\varphi_a) \cdot \vec{n} = \frac{\sigma(x)}{\varepsilon_0}$, where ε_s is the dielectric permittivity of the substrate, $\sigma(x)$ is the surface charge density on the substrate, $\vec{n}$ is the normal vector of the substrate, and φ_s and φ_a are the electrostatic potentials infinitesimally away from the solid surface inside the substrate and inside air, respectively. To complete the set of boundary conditions, we assume that the surrounding circular boundaries are far away and that the normal component of the electric field vanishes in the far field, $\vec{\nabla}\varphi_{farfield} \cdot \vec{n} = 0$. We further assume that the electrode below the substrate is grounded, $\varphi_{electrode} = 0$. After the electric field fulfilling the equations and the boundary conditions above is obtained, the electrostatic force acting on the drop can be calculated from the integral of the Maxwell stress tensor on the drop's surface $F_e = \frac{\varepsilon_0}{2} \int_{drop} \vec{E}^2 \, \vec{n} \cdot \vec{n}_x ds$, where $\vec{n}_x$ is the normal vector pointing in sliding direction.

We implemented the equations and boundary conditions above in variational form into the open-source software package FEniCS [26]. The solution was obtained by the common finite-element method. To determine the potential on the drop surface φ_{drop} we solved a tracking-type optimal control problem utilizing *dolfin-adjoint* to automatically compute the gradient [27]. The finite-element mesh was generated with *Gmsh* (https://gmsh.info/). The mesh was systematically refined around the substrate-air interface as well as the drop-air interface with cell sizes as low as 50 µm. In the contact line region the minimal cell size was only 50 nm, see the right inset in figure S13.

The problem parameters include the drop shape and size, contact angle, sliding length, charge distribution, substrate thickness, and dielectric permittivity of the solid. Here, we consider a fixed, circular-arc shaped drop with contact angles $\Theta_a = \Theta_r = 90°$ and diameter $w = 4$ mm on a substrate with $\varepsilon_s = 3.9$. The charge density behind the drop is supposed to be homogenous and constant at σ = 5 µC/m^2. There is no surface charge ahead of the drop. The resulting electrostatic force is plotted versus the sliding length L in figure S14 (symbols) for different substrate thicknesses. The electrostatic force scales linearly with slide length. With decreasing thickness of the substrate, the screening influence of the electrode becomes stronger, which results in lower overall electrostatic forces acting on the drop.

In figure S14 we also compare electrostatic forces calculated with the analytical model (black lines, Eq. S5) with the numerically calculated forces (symbols). The analytical model and the simulations predict the same linear scaling of the force with the sliding length. As long as h is small the influence of h on the resulting force is negligible (lines, Figure S14); therefore, we set h=0. Furthermore, it turned out that, by shifting the effective drop charge away from the drop's center to different horizontal positions a, the analytical model can fit the simulations. Thus, phenomenologically we can take the presence of a back-electrode into account by choosing the right value of a. One reason for this could be that for a vanishing substrate thickness the charge on the drop surface is symmetrically distributed (which results in a vanishing horizontal force on the drop, compare the smaller forces for thinner substrates in Figure S14), whereas for larger thicknesses the charges on the substrate induce significant charges at the rear end of the drop. In addition, our simulations show that a large fraction of the charges is located in the utmost vicinity of the contact line.

In summary, the numerical calculations confirm the validity and scaling of Eq. (5). Good agreement was achieved when the center of charge of the drop was placed directly on the surface (h = 0). The choice of the parameter a is dictated by the thickness of the substrate. We find that for 1 mm and 5 mm thick substrates, setting $a = 2$ mm and $a = 0.8$ mm, respectively, can mimic the shielding effect of the back electrode.

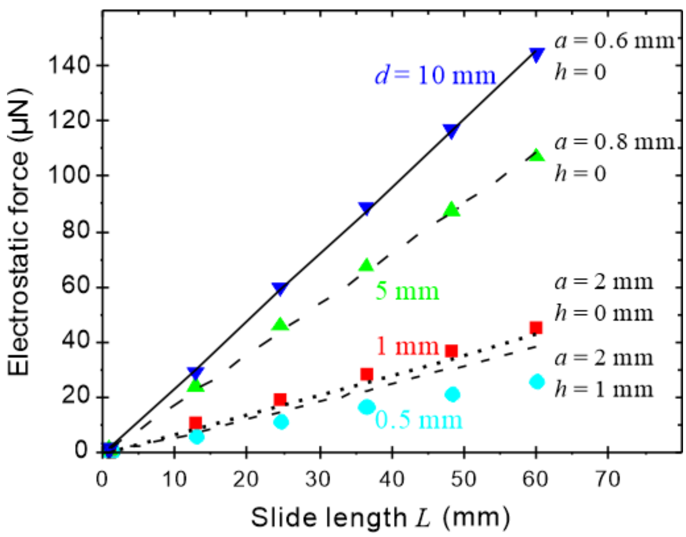

***Figure S14**. Electrostatic force on a drop calculated from the solution of Poisson's equation (symbols) and the analytical model for different positions of the effective point charge (eq. S6, lines) as well as slide lengths L and substrate thicknesses d. Here we assumed a constant charge density for the deposited charge of $\sigma_1 = 5$ µC/m² behind the drop.*

S13. Drop velocity profiles on conducting and high-permittivity substrates of PS, Teflon, PDMS, and thiol-coated surfaces

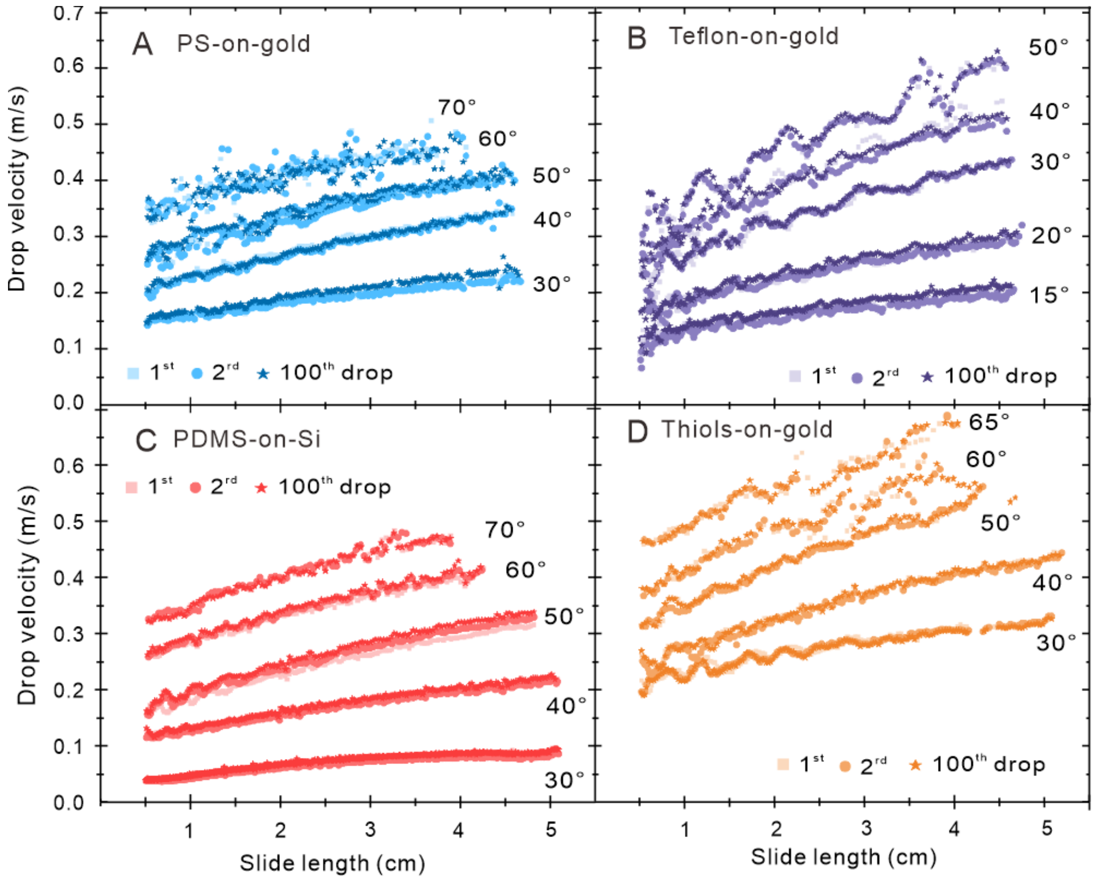

Figure S15*. Representative results for drop velocity-versus-slide length measured at different tilt angles. (A) 20 nm PS films on gold, (B) 60 nm thick Teflon films on gold, (C) PDMS on silicon wafers, and (D) Perfluorodecanethiol on gold. Results for drop number 1 (rectangle), 2 (circle), and 100 (star) are plotted. The lower tilt angle was given by the requirement that drops slide at all; at lower tilt angels the drops did not move. The maximal tilt angle was given by the requirement of having a stable steady state shape of the drop. At higher tilt angles and thus higher velocities the drop shape analysis started to fail.*

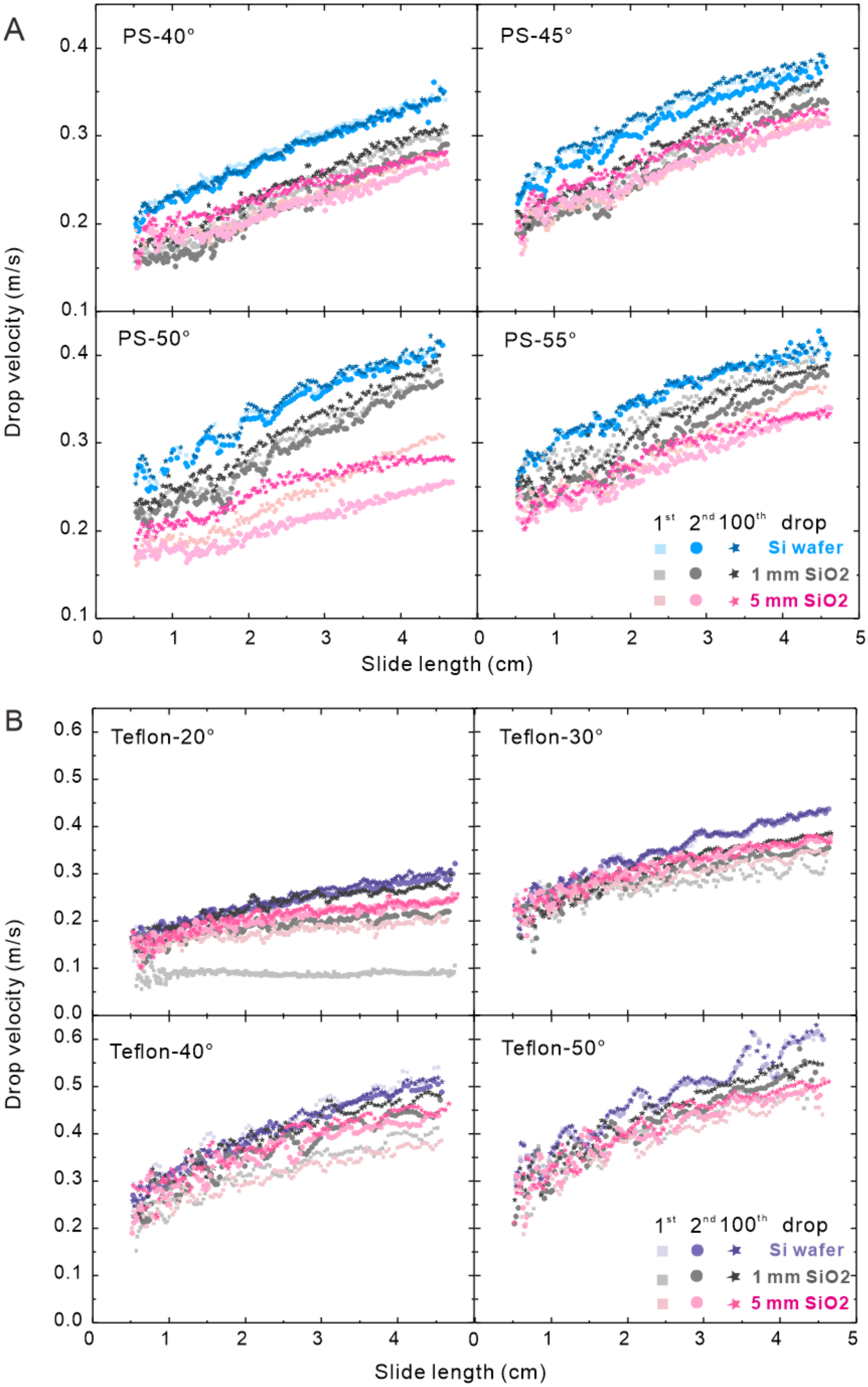
A
PS-40°
PS-45°
PS-50°
PS-55°
Drop velocity (m/s)
Slide length (cm)
1st 2nd 100th drop
Si wafer
1 mm SiO2
5 mm SiO2
B
Teflon-20°
Teflon-30°
Teflon-40°
Teflon-50°
Drop velocity (m/s)
Slide length (cm)
1st 2nd 100th drop
Si wafer
1 mm SiO2
5 mm SiO2

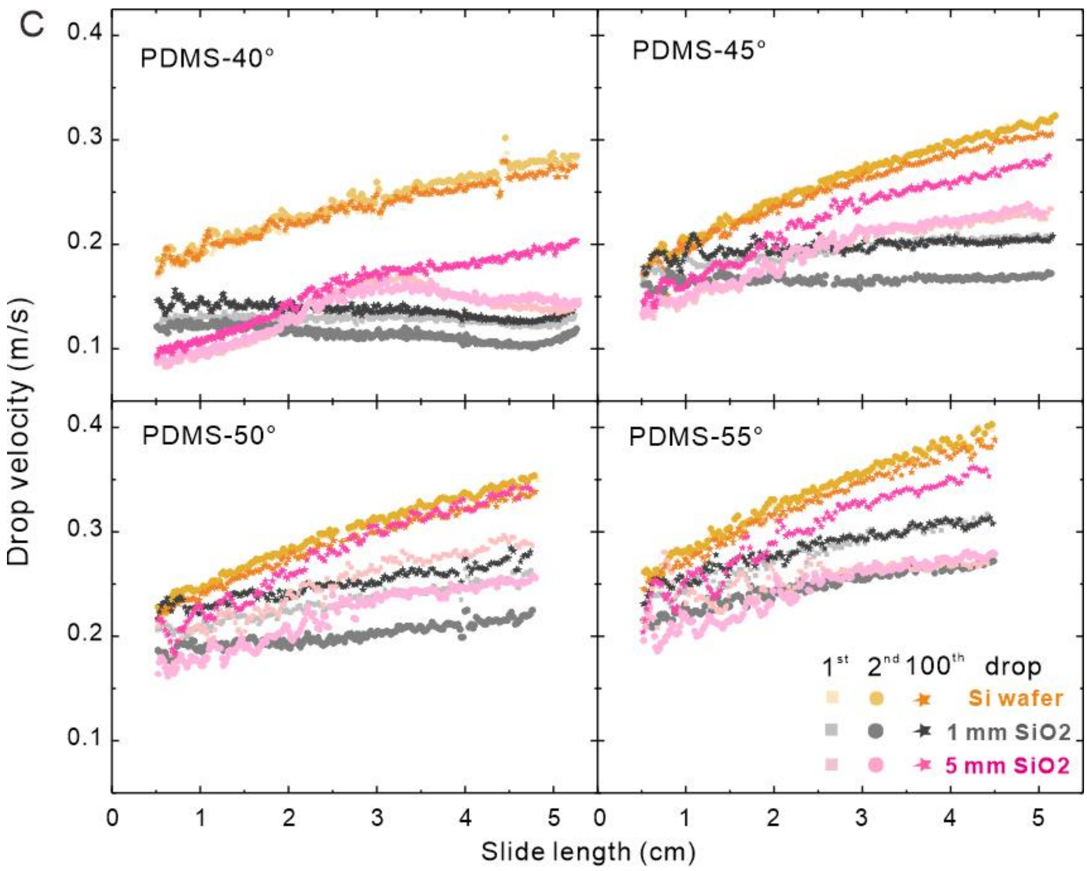

Figure S16. *Representative results for drop velocity-versus-slide length measured at different tilt angles. (A) 20 nm PS films, (B) 60 nm thick Teflon films, and (C) PDMS on 1 mm* SiO_2 *(blue symbols) and 5 mm* SiO_2 *(red symbols). For comparison also the results obtained on Si wafers (A) or gold (B, C) are plotted as black symbols. Results for drop number 1 (rectangle), 2 (circle), and 100 (star) are plotted.*

S14. Reference forces for PS, Teflon, PDMS, and thiol-coated surfaces

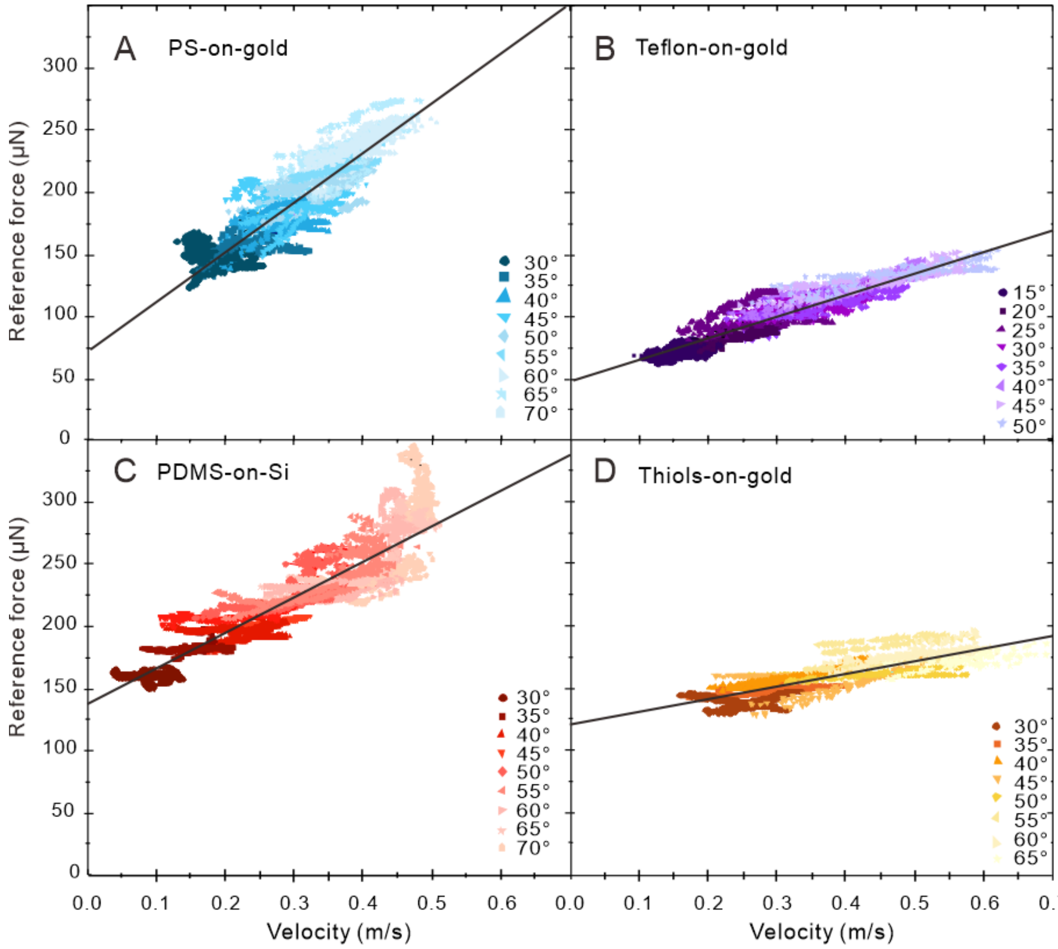

Figure S17. *Reference forces measured on different substrates and the linear fit (black lines) derived from velocities up to 0.4 m/s. (A) PS-on-gold fitted by* $F_r = 74\ \mu N + 398\,\frac{\mu N s}{m} \cdot U$*, (B) Teflon-on-gold fitted with* $F_r = 48\ \mu N + 175\,\frac{\mu N s}{m} \cdot U$ *, (C) PDMS-on-Si fitted by* $F_r = 141\ \mu N + 269\,\frac{\mu N s}{m} \cdot U$*, and (D) thiols-on-gold fitted with* $F_r = 120\ \mu N + 103\,\frac{\mu N s}{m} \cdot U$*. The water drops of 33 µL volume were deposited at 1.3 s intervals. The results were obtained from the respective 2*nd *and 10*th *drop for tilt angles of between 15 and 70°. To complete the graph in particular at high velocity we added results obtained from 10-14 cm slide distance, where the drops had reached or were close to their steady state velocity.*

S15. Measured extra forces of drops on PS, Teflon, and PDMS-coated surfaces

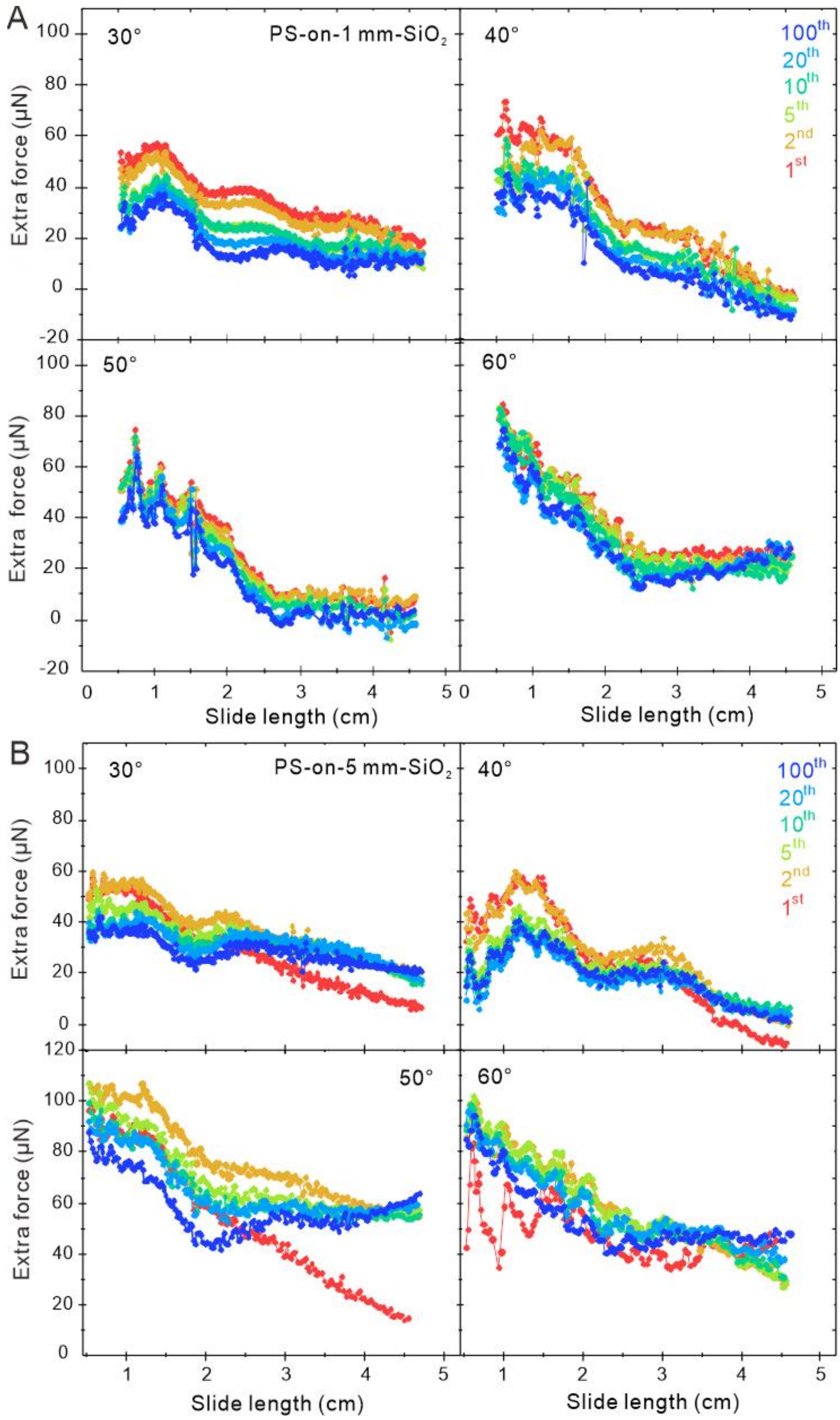

***Figure S18**. (A) Examples for extra forces acting on water drops sliding down PS-on-1mm-SiO_2 and (B) PS-on-5mm-SiO_2 for different tilt angles. Plotted are results for the 1st, 2nd, 5th, 10th, 20th, and the 100th drop. 33 µL drops were deposited at an interval of 1.3 s. Force were calculated with Eq. (1) using m*/m=1.05 and* $F_r = 74\ \mu N + 398 \frac{\mu N s}{m} \cdot U$.

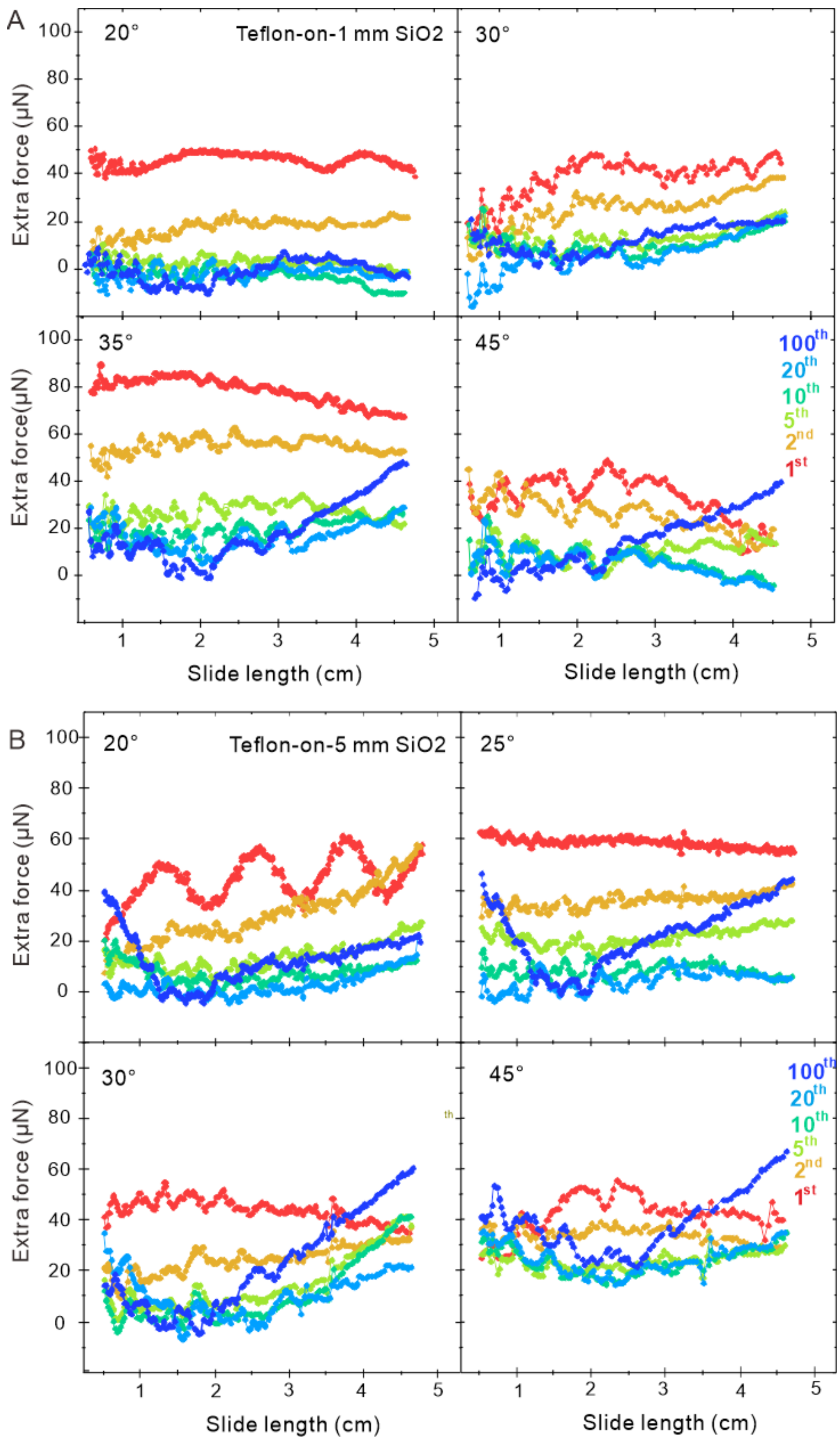

Figure S19. *(A) Examples for extra forces acting on water drops sliding down Teflon-on-1mm-SiO_2 and (B) Teflon-on-5mm-SiO_2. For different tilt angles. Plotted are results for the 1^{st}, 2^{nd}, 5^{th}, 10^{th}, 20^{th}, and the 100^{th} drop. 33 µL drops were deposited at an interval of 1.3 s. Force were calculated with Eq. (1) using m*/m=*1.05 *and* $F_r = 48\ \mu N + 175 \frac{\mu N s}{m} \cdot U$.

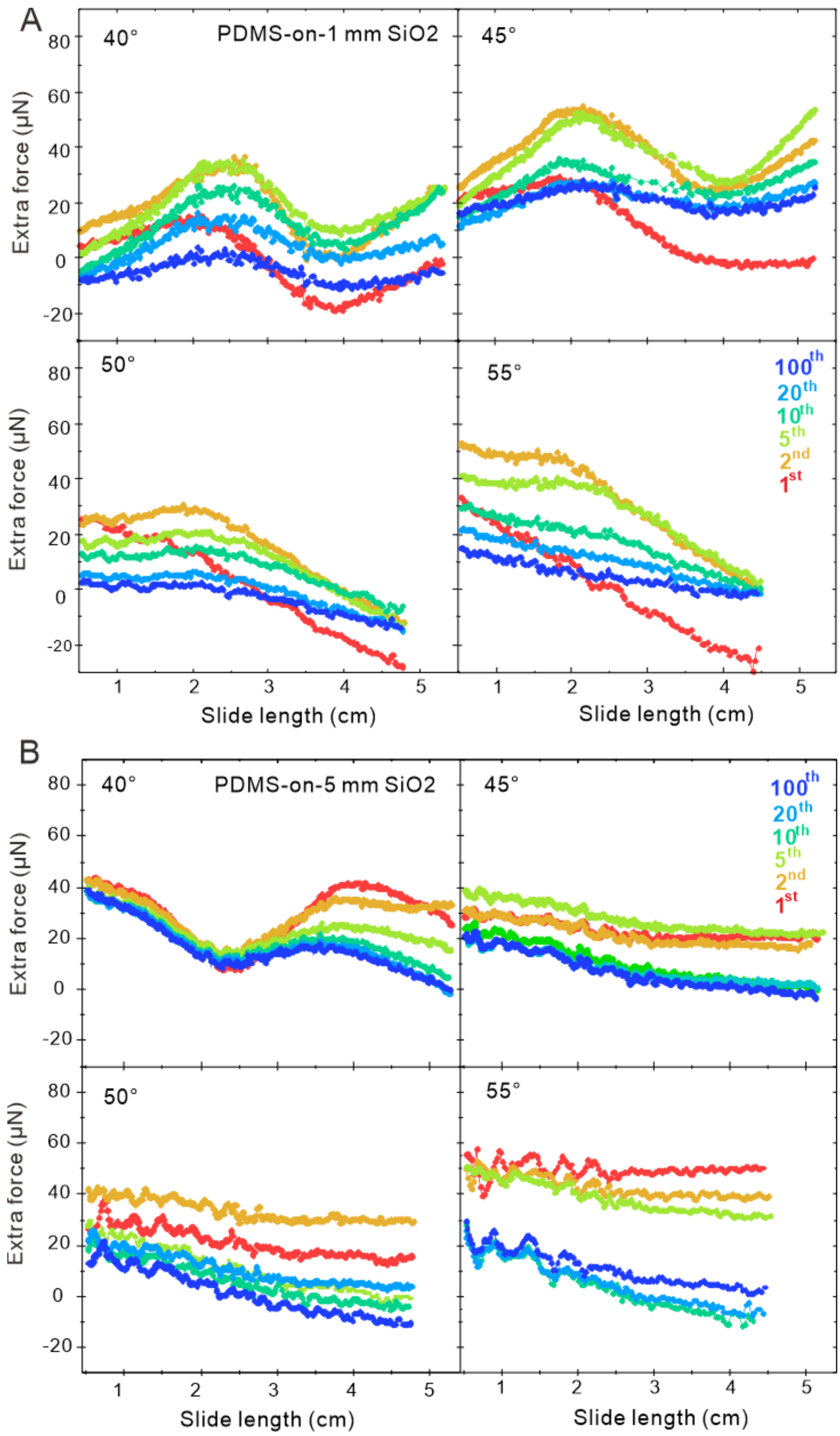

Figure S20. *(A) Examples for extra forces acting on water drops sliding down PDMS-on-1mm-SiO_2 and (B) PDMS-on-5mm-SiO_2 for different tilt angles. Plotted are results for the 1^{st}, 2^{nd}, 5^{th}, 10^{th}, 20^{th}, and the 100^{th} drop. 33 µL drops were deposited at intervals of 1.3 s. Force were calculated with Eq. (3) using m*/m=1.05 and* $F_r = 141\ \mu N + 269 \frac{\mu N s}{m} \cdot U$.

References

1 Le Grand, N., Daerr, A. & Limat, L. Shape and motion of drops sliding down an inclined plane. *J. Fluid Mech.* **541**, 293-315 (2005).

2 Kim, H. Y., Lee, H. J. & Kang, B. H. Sliding of liquid drops down an inclined solid surface. *J. Colloid Interface Sci.* **247**, 372-380 (2002).

3 Huh, C. & Scriven, L. E. Hydrodynamic model of steady movement of a solid/liquid/fluid contact line. *J. Colloid Interface Sci.* **35**, 85-101 (1971).

4 Voinov, O. V. Hydrodynamics of wetting. *Fluid Dynamics* **11**, 714-721 (1976).

5 Cox, R. G. The dynamics of the spreading of liquids on a solid surface. Part 1. Viscous flow. *J. Fluid Mech.* **168**, 169-194 (1986).

6 Dussan, E. B., Ramé, E. & Garoff, S. On identifying the appropriate boundary conditions at a moving contact line: an experimental investigation. *J. Fluid Mech.* **230**, 97-116 (1991).

7 Eggers, J. & Stone, H. A. Characteristic lengths at moving contact lines for a perfectly wetting fluid: the influence of speed on the dynamic contact angle. *J. Fluid Mech.* **505**, 309-321 (2004).

8 Eggers, J. Existence of receding and advancing contact lines. *Phys. Fluids* **17**, 082106 (2005).

9 Snoeijer, J. H. Free-surface flows with large slopes: Beyond lubrication theory. *Physics of Fluids* **18**, 021701 (2006).

10 Maglio, M. & Legendre, D. in *Computational and Experimental Fluid Mechanics with Applications to Physics, Engineering and the Environment Environmental Science and Engineering* (eds L. D. Sigalotti, J. Klapp, & E. Sira) 47-69 (2014).

11 Andersen, N. K. & Taboryski, R. Drop shape analysis for determination of dynamic contact angles by double sided elliptical fitting method. *Measurement Science and Technology* **28**, 047003 (2017).

12 Li, X. *et al.* Adaptation of a styrene-acrylic acid copolymer surface to water. *Langmuir* **37**, 1571–1577 (2021).

13 Yarnold, G. D. The motion of a mercury index in a capillary tube. *Proceedings of the Physical Society* **50**, 540-552 (1938).

14 Frenkel, Y. I. On the behavior of liquid drops on a solid surface. 1. The sliding of drops on an inclined surface. *J. Exptl. Theoret. Phys. (USSR)* **18**, 659-669 (1948).

15 Dussan, E. B. & Davis, S. H. On the motion of a fluid-fluid interface along a solid surface. *J. Fluid Mech.* **65**, 71-95 (1974).

16 de Gennes, P. G. Wetting: Statics and dynamics. *Rev. Modern Phys.* **57**, 827-863 (1985).

17 Shikhmurzaev, Y. D. The moving contact line on a smooth solid surface. *Int. J. Multiphase Flow* **19**, 589-610 (1993).

18 Olin, P., Lindstrom, S. B., Pettersson, T. & Wagberg, L. Water drop friction on superhydrophobic surfaces. *Langmuir* **29**, 9079-9089 (2013).

19 Yilbas, B. S., Al-Sharafi, A., Ali, H. & Al-Aqeeli, N. Dynamics of a water droplet on a hydrophobic inclined surface: influence of droplet size and surface inclination angle on droplet rolling. *RSC Advances* **7**, 48806-48818 (2017).

20 Sartori, P. *et al.* Drop motion induced by vertical vibrations. *New J. Phys.* **17**, 113017 (2015).

21 Ngan, C. G. & Dussan, E. B. On the dynamics of liquid spreading on solid surfaces. *J. Fluid Mech.* **209**, 191-226 (1989).

22 Yue, P. T. Thermodynamically consistent phase-field modelling of contact angle hysteresis. *J. Fluid Mech.* **899**, A15-41 (2020).

23 Cai, X., Marschall, H., Wörner, M. & Deutschmann, O. Numerical simulation of wetting phenomena with a phase-field method using OpenFOAM. *Chemical Engineering & Technology* **38**, 1985-1992 (2015).

24 Jamshidi, F. *et al.* On suitability of phase-field and algebraic volume-of-fluid OpenFOAM (R) solvers for gas-liquid microfluidic applications. *Computer Physics Communications* **236**, 72-85 (2019).

25 Stetten, A. Z., Golovko, D. S., Weber, S. A. L. & Butt, H. J. Slide electrification: charging of surfaces by moving water drops. *Soft Matter* **15**, 8667-8679 (2019).

26 Alnaes, M. S. *et al.* The FEniCS Project Version 1.5. *Archive of Numerical Software* **3**, 9-23 (2015).

27 Mitusch, S. K., Funke, S. W. & Dokken, J. S. dolfin-adjoint 2018.1: automated adjoints for FEniCSand Firedrake. *The Journal of Open Source Software* **4**, 1292 (2019).